JGR Atmospheres

RESEARCH ARTICLE
10.1029/2018JD028963

Radiative Influence of Horizontally Oriented Ice Crystals over Summit, Greenland

Robert A. Stillwell[1,2,3], Ryan R. Neely III[4], Jeffrey P. Thayer[3], Von P. Walden[5], Matthew D. Shupe[6,7], and Nathaniel B. Miller[6,7]

[1]Advanced Study Program, National Center for Atmospheric Research, Boulder, CO, USA, [2]Earth Observing Laboratory, National Center for Atmospheric Research, Boulder, CO, USA, [3]Ann and H.J. Smead Department of Aerospace Engineering Sciences, University of Colorado, Boulder, CO, USA, [4]National Centre for Atmospheric Science and the School of Earth and Environment, University of Leeds, England, UK, [5]Department of Civil and Environmental Engineering, Laboratory for Atmospheric Research, Washington State University, Pullman, WA, USA, [6]Cooperative Institute for Research in Environmental Sciences, University of Colorado, Boulder, CO, USA, [7]Physical Sciences Division, Earth System Research Laboratory, National Oceanic and Atmospheric Administration, Boulder, CO, USA

Key Points:
- First long-term observational study of the radiative importance of ice crystal orientation in the polar regions is presented
- Ice clouds containing oriented crystals show greater radiative effect than clouds without oriented crystals in the shortwave and longwave
- Observations suggesting enhanced radiative effect of oriented ice crystals occurring in the longwave require further investigation

Correspondence to:
R. A. Stillwell,
robert.stillwell@colorado.edu

Citation:
Stillwell, R. A., Neely III, R. R., Thayer, J. P., Walden, V. P., Shupe, M. D., & Miller, N. B. (2019). Radiative influence of horizontally oriented ice crystals over summit, greenland. *Journal of Geophysical Research: Atmospheres*, *124*, 12,141–12,156. https://doi.org/10.1029/2018JD028963

Received 7 MAY 2018
Accepted 17 OCT 2019
Accepted article online 26 OCT 2019
Published online 17 NOV 2019

Abstract Ice crystals commonly adopt a horizontal orientation under certain aerodynamic and electrodynamic conditions that occur in the atmosphere. While the radiative impact of horizontally oriented ice crystals (HOIC) has been theoretically studied with respect to their impact on shortwave cloud albedo, the longwave impact remains unexplored. This work analyzes the occurrence of HOIC at Summit, Greenland, from July 2015 to June 2017. Using polarization lidar and ancillary atmospheric sensors, ice crystal orientations are identified and used to interpret cloud radiative impact on the surface radiation budget. We find HOIC occur in at least 25.6% of all ice-only column observations. We find that the shortwave impact of HOIC is to increase cloud radiative effect by approximately 22% for a given solar zenith angle. We also find that the longwave impact of HOIC compared to randomly oriented ice crystals are statistically different at the $p < 0.01$ significance level, increasing the surface radiative effect by approximately 8% for clouds with infrared optical depths < ~1. We suggest that the observed difference between the surface radiative effect for clouds containing randomly oriented ice crystals and HOIC may be due to enhanced scattering, but this hypothesis needs to be further explored with more detailed observations and modeling.

Plain Language Summary Because of their shape, ice crystals can fall from clouds with a preferential horizontal orientation due to drag forces acting on their surfaces. Using novel remote sensing techniques, we identify the occurrence of preferentially oriented ice crystals and attempt to quantify the impact of ice crystal orientation on the surface environment at a field site in the Arctic. We observe, to our knowledge, for the first time, statistically significant differences in the radiative properties of ice clouds containing preferentially oriented ice crystals from those containing no detectable preferentially oriented ice crystals. We suggest a hypothesis that may explain this difference, but note it requires further testing to fully analyze and define methods to explore the mechanism further.

1. Introduction

The influence of clouds on the surface energy budget is referred to as the cloud radiative effect (CRE). Clouds warm the surface by emitting longwave (LW) radiation but also cool it by reflecting incoming shortwave (SW) radiation. CRE depends strongly on both the microphysical and macrophysical properties of the cloud including optical depth (OD), phase, and temperature, as well as environmental conditions such as solar zenith angle (SZA), underlying surface albedo, and surface temperature (Corti & Peter, 2009; Cox et al., 2014; Curry & Ebert, 1992; Ramanathan et al., 1989; Shupe & Intrieri, 2004). On average, clouds cool the surface globally (Matus & L'Ecuyer, 2017). However, in the polar regions where surface albedo is significantly higher than the global average, clouds generally warm the surface, except in the summer when the minimum SZAs and surface albedo occur (Curry & Ebert, 1992; Intrieri et al., 2002; Kay & L'Ecuyer, 2013). At sites with high year-round surface albedo, this cooling effect is minimized. Miller et al. (2015) found that over the central Greenland ice sheet (GrIS), clouds almost always warm the surface even in the summer with minimum SZAs.

Characterizing the determining factors of cloud OD is essential for understanding CRE. These factors include the vertical distribution, concentration, phase, size, and orientation of the population of hydrometeors (Curry & Ebert, 1992). Larger OD increases cloud albedo but also increases the opacity to outgoing LW radiation (Chen et al., 2000). Microphysical composition, whether liquid, ice, or both, has a significant impact on a cloud's radiative properties (Matus & L'Ecuyer, 2017; Morrison et al., 2012; Shupe & Intrieri, 2004). Sun and Shine (1994) found that the amount of radiation reflected from liquid clouds is between two and four times the amount reflected by ice clouds given the same total water path and SZA. This is largely due to microphysical differences between populations of cloud liquid and ice particles. Ice crystals within a cloud are typically larger, and less numerous, than liquid droplets (Shupe & Intrieri, 2004). This size difference causes less surface area per unit water and decreases the overall OD unless compensated for by other mechanisms, such as preferential orientation. Although the relationship between size and concentration is significant in both liquid and ice clouds, preferential orientation, a property specific to ice crystals, is also an important consideration. As a result of their asymmetry, the orientation of ice crystals significantly affects their interaction with incident radiation and therefore affects the resulting CRE (Hirakata et al., 2014).

Ice crystals with Reynolds numbers between ~1 and ~100 are known to adopt a preferred orientation in the atmosphere due to drag forces encountered when falling (Keat & Westbrook, 2017; Klett, 1995; Platt, 1978; Sassen, 1980, 1984; Takano & Liou, 1989, 1993; Thomas & Cartwright, 1990; Tricker, 1971; Westbrook et al., 2010; Whipple, 1940). The preferred orientation is typically horizontal with its largest surface area parallel to the Earth's surface (Hashino et al., 2014; Ji & Wang, 1999; Kajikawa, 1992). Although ice crystal habits, such as Parry-oriented columns, are known to adopt the same kind of preferred orientation (Sassen & Takano, 2000; Thomas & Cartwright, 1990), horizontally oriented ice crystals (HOIC) are typically thought to have planar habits with significantly faceted areas (i.e., hexagonal or stellar plates and branched or dendritic planar crystals) (Bréon & Dubrulle, 2004; Westbrook et al., 2010). Ice crystals are also well known to adopt orientations due to electric fields in clouds (Foster & Hallett, 2002; Vonnegut, 1965).

The orientation of ice crystals within Arctic clouds has recently been explored using the space-borne Cloud-Aerosol Lidar with Orthogonal Polarization (CALIOP) (e.g., Yoshida et al., 2010). Using 18 months of CALIOP observations, Noel and Chepfer (2010) found over 50% of optically thin ice clouds exhibit characteristics indicative of the presence of HOIC in the Arctic. Zhou et al. (2013) extended this work to look at both ice and mixed-phase cloud layers and similarly found that ~40% of clouds over the Arctic contain a significant population of HOIC. In addition, both found that the occurrence of HOIC is strongly dependent on cloud temperature, and by extension ice crystal habit, with a decline in occurrence at temperatures below -30°*C*. Zhou et al. (2013) showed that this dependence is much more significant for ice-only clouds. They also confirm, on a global scale, the results of Westbrook et al. (2010) made at the Chilbolton Observatory. These results show that, though HOIC can be found in cold ice clouds, HOIC are more common in warm ice and mixed-phase clouds like those observed throughout the Arctic (Field et al., 2004; Hogan et al., 2003; Shupe, 2011; Shupe et al., 2011; Westbrook et al., 2010).

Turbulence and vertical motion within a cloud are a defining characteristic of Arctic mixed-phase clouds (Morrison et al., 2012) and are known to be essential for their maintenance (Shupe et al., 2008). Such motions seem contrary to the conditions required for ice crystal orientation but have been found through theory and observation to have little impact (Breon & Dubrulle, 2004; Klett, 1995; Westbrook et al., 2010). For typically observed turbulent dissipation rates, the velocity perturbations across ice crystal faces are found to be ~50 times smaller than their fall speed (Westbrook et al., 2010).

We hypothesize that the presence of HOIC will impact the surface and top-of-atmosphere (TOA) energy balance in both SW and LW. HOIC have been theorized to increase cloud SW albedo by as much as 40% (Takano & Liou, 1989). To our knowledge, only the impact of HOIC on incoming SW radiation has been reported (Hess & Wiegner, 1994; Sassen et al., 2003; Takano & Liou, 1989). There have been no previous observational studies exploring the CRE implications of clouds with and without HOIC on both SW and LW radiation at the surface or TOA, though the anisotropic scattering of HOIC is well established via modeling studies.

2. Methods and Data Sources

Noel and Chepfer (2010) and Zhou et al. (2013) separate populations of HOIC from randomly oriented ice crystals (ROIC) by comparing observations containing specular and non-specular reflections, respectively.

Table 1
Summary of Data Products Used for This Study and the Resolutions at Which They Are Natively Acquired

Instrument	Product used	Product type	Uptime[a]	Vertical resolution	Temporal resolution	Reference
CAPABL	•Classification	•RR	97.9%	25.4 m	~82 s	Neely et al., 2013
	•CSCI	•Column				Stillwell et al., 2018
MMCR	•Doppler moments	•RR	97.5%	87.5 m	~8 s	Moran et al. 1998
	•IWC	•RR				Clothiaux et al. 1999
	•IWP	•Column				Shupe et al., 2005
MWR	•LWP	•Column	62.1%	See Miller et al., 2013	~100 s	Turner et al., 2007
	•PWV	•Column				Cadeddu et al., 2013
	•Temperature	•RR				Miller et al., 2013
P-AERI	•10.4 μm radiance	•Column	97.5%	----------	~25 s	Knuteson et al., 2004a
	•IR OD	•Column				Knuteson et al., 2004b
Radiosonde	•Temperature	•RR	96.7%	~5 m	12 hr	Shupe et al., 2013
	•Pressure	•RR				
	•Relative humidity	•RR				
Ozonesonde	•O_3 number density	•RR	91.4%	100 m	Weekly	NOAAOZWV, 2017
Flask samples	•CO_2	•Point	100%	----------	Monthly	Dlugokencky et al., 2017
Broadband radiation	•0.285–2.8 μm irradiance	•Hem	98.1%	----------	60 s	NOAAGRAD, 2017
	•3.5–50 μm irradiance	•Hem				

Note: References further describing the definition or detail of these products are also provided. Abbreviations: RR = range resolved; Hem = hemispheric.
[a]Note that here we consider continuously running instruments like CAPABL, MMCR, MWR, P-AERI, and Broadband Radiation "up" if the instrument is actively taking data, running automated housekeeping, or running automated calibration scans. Non-automated actions are not included. For intermittent measurements, like sondes and flask samples, we take the number of expected measurements vs. the number actually collected.

Advancements in polarimetric active remote sensing have allowed for HOIC to be unambiguously identified with a single instrument without requiring specular reflections (Hayman et al., 2012, 2014; Hayman & Thayer, 2012). Neely et al. (2013) and Stillwell et al. (2018) have utilized these advancements to observe HOIC over the GrIS as part of the Integrated Characterization of Energy, Clouds, Atmospheric state, and Precipitation at Summit (ICECAPS) project.

Summit, Greenland, is located 3212 m above mean sea level (AMSL) on top of the GrIS at 72.6°N, 38.5°W. In 2010, the ICECAPS project established an intensive cloud observatory at Summit capable of measuring atmospheric turbulent and thermodynamic properties as well as cloud properties (Shupe et al., 2013). Here, we use observations from ICECAPS and NOAA Earth System Research Laboratory Global Monitoring Division (GMD) in conjunction with estimates of clear-sky fluxes calculated by the Rapid Radiative Transfer Model (RRTM) to assess the CRE of HOIC over Summit from July 2015 to June 2017.

2.1. Data Sources

The ICECAPS instrumentation includes the Cloud Aerosol Polarization and Backscatter Lidar (CAPABL), twice-daily radiosonde profiles, the Polar Atmospheric Emitted Radiance Interferometer (P-AERI), the Millimeter Cloud Radar (MMCR), and a pair of microwave radiometers (MWRs). In addition to ICECAPS measurements, we also use GMD's observation of stratospheric ozone (O_3), broadband solar and thermal irradiance, and surface CO_2. A list of relevant instruments, instrument uptime, and resolutions is given in Table 1 and described here in more detail.

Assessment of cloud phase and ice crystal orientation is made using CAPABL, the only instrument at Summit capable of unambiguously identifying HOIC. To identify HOIC, CAPABL makes observations of diattenuation and depolarization using the theory of Hayman and Thayer (2012). HOIC exhibit nonzero values of both depolarization and diattenuation when observed at oblique angles, while ROIC only exhibit nonzero values of depolarization (Neely et al., 2013). This information is used to classify range resolved observations as clear-air, liquid-containing, ROIC, or HOIC voxels. The range resolved data classification is aggregated into a single column identification (hereafter the CAPABL single column identification or CSCI) to specify if the atmospheric column overhead contains clear-air, liquid, ROIC, or HOIC and to facilitate the interpretation of non-range resolved measurements. Both classifications are described by Stillwell et al. (2018) and are used without modification. This procedure is summarized in Appendix A for reference. Note that pure liquid-containing clouds are rare at Summit. Liquid identifications almost always contain a subpopulation of ice that is unresolvable. Thus, liquid voxels/columns almost exclusively contain mixed-

phase voxels/columns. Hereafter, liquid, as described by Stillwell et al. (2018), is referred to as mixed-phase to more accurately represent their physical state.

Refinement of the CSCI is achieved using MWR data. Column integrated liquid water path (LWP) and precipitable water vapor are retrieved using physical retrievals (Turner et al., 2007) and optimal estimation of microwave brightness temperatures (Cadeddu et al., 2013). LWP is used to evaluate the CSCI where columns identified as mixed-phase must contain a nonzero LWP (i.e., LWP above the retrieval uncertainty, ~5 g/m^2), and columns labeled clear-air, ROIC, or HOIC must have zero LWP (below retrieval uncertainty).

To estimate the clear-sky fluxes necessary to calculate CRE, an assessment of the vertical profile of atmospheric temperature and moisture is provided up to ~25 km AMSL from twice-daily radiosonde profiles. Above the height of individual radiosonde profiles, the thermodynamic structure is estimated using forecasts from the European Center for Medium-Range Weather Forecasts (ECMWF) and the NRLMSIS-00 model (Hedin, 1985; Labitzke et al., 1985; Picone et al., 2002). Precipitable water vapor measurements are used to scale humidity profile measurements as described by Miller et al. (2015). In the lowest kilometer above the surface, the temperature profiles between radiosonde profiles are retrieved from MWR data as described by Miller et al. (2013).

Clear-sky flux estimates also require an estimate of the concentration of several trace gases. We utilize monthly surface flask sample measurements (Dlugokencky et al., 2017) to estimate a vertically constant CO_2 mixing ratio. O_3 mixing ratio profiles from the surface to the stratosphere are estimated from weekly ozonesondes (NOAAOZWV, 2017). N_2O, CO, CH_4, and O_2 concentrations are estimated from a standard profile for subarctic winter conditions (McClatchey et al., 1972).

The P-AERI observes downwelling spectral radiance in a range of 3 to 19 μm at sub-minute resolution (Knuteson et al., 2004a, 2004b). We use observations from the P-AERI to further refine the CSCI and make an approximation of cloud infrared (IR) OD. Specifically, we use P-AERI spectral radiance in the 10.4-μm microwindow (a 5-nm, 0.5-cm^{-1}, wide representative "clear window" with minimal atmospheric emission) to evaluate the clear-air CSCI. We require all classified clear-air columns to have atmospheric emission at 10.4 μm <2 $mW/m^2/sr/cm^{-1}$.

To estimate the IR OD, we first use CAPABL's range resolved data identifications and reflectivity from the 35-GHz MMCR general mode to estimate cloud boundaries. MMCR data with SNR exceeding -14 dB are used. With temperature values described above, the emission temperature of the cloud at the base, top, and geometric median altitude is estimated. From that emission temperature, cloud IR OD is inferred from emission spectra measured by P-AERI. The IR OD of optically thick clouds is well described by the emission from the cloud base temperature. However, the emission temperature is difficult to determine in optically thin clouds; therefore, the temperature at cloud base and top is used to bound this uncertainty in the IR OD.

Further, refinement of the CSCI is achieved by using the calculated IR OD. Of concern is a bias introduced by not observing the whole ice column due to lidar extinction, possibly altering the interpretation of some ice columns between ROIC and HOIC classifications. HOIC are expected to exist in narrow temperature ranges, which means that they could be vertically stratified. Stillwell et al. (2018) note that CAPABL observed approximately 75% of all ice voxels observed by the MMCR. As a precaution, columns labeled as ROIC or HOIC with IR OD >1.5 are removed to avoid any possible bias resulting from incomplete ice column observations.

The radiative impact of ROIC and HOIC is assessed using broadband solar and thermal irradiances. A pair of pyrgeometers with sensitivity from ~3.5 to 50 μm are used to observe the upwelling and downwelling thermal emissions (LW↑ and LW↓) (Miller et al., 2015; NOAAGRAD, 2017). The upwelling and downwelling solar irradiances (SW↑ and SW↓) are measured by a pair of pyranometers, with sensitivity from 0.285 to 2.8 μm (Miller et al., 2015; NOAAGRAD, 2017). Riming and frosting are minimized by aspirating the instruments, pyranometers with heated air and the pyrgeometers with ambient air, and daily checks.

Finally, MMCR data are used to quantify any possible radiative bias caused by the total quantity of ice in a cloud. MMCR reflectivity data are used to calculate ice water content (IWC) per radar voxel using the power-law method of Shupe et al. (2005). The *a* coefficient described by Shupe et al. (2005) is found by linearly interpolating between monthly average values described in that work (summarized in their Figure 2). Voxel IWC is then integrated over the whole column to yield ice water path (IWP).

2.2. Data Interpolation

The data described above are all collected at different temporal and spatial resolutions, summarized in Table 1. To facilitate the analysis, all data are interpolated to the CAPABL scale as described by Stillwell et al. (2018). Range resolved measurements such as those from radiosondes, MWR-derived temperature profiles, and ozonesondes are merged with model data, as described by Miller et al. (2015), to an altitude of ~58 km AMSL. Data are then interpolated in two dimensions to CAPABL's data scale. Column and hemispheric measurements such as those from PAERI, MWR, and broadband irradiances are incoherently averaged to a similar time scale and then linearly interpolated to CAPABL's time scale. After interpolation, all data have a temporal resolution of approximately 82 s and range resolved measurements have a vertical resolution of approximately 25 m. Data are only used if CAPABL has valid data to classify the atmosphere for a given time period.

2.3. RRTM

Clear-sky broadband irradiances, $LW{\uparrow}_{CS}$, $LW{\downarrow}_{CS}$, $SW{\uparrow}_{CS}$, and $SW{\downarrow}_{CS}$, are estimated using RRTM (Clough et al., 2005; Mlawer et al., 1997) at 1-min resolution to match the broadband radiation measurements. The calculations were performed following the method described in Miller et al. (2015) with data described in section 2.1. Deviations from this method include (1) the temporal resolution at which we calculated the clear-sky fluxes, and (2) when data are unavailable, steps requiring missing data are not performed except when ECMWF data were unavailable, NRLMSIS-00 data are substituted. We calculate fluxes at 75 levels throughout the atmosphere but only report surface values. The difference in modeled data has been examined (not shown) but no major qualitative or quantitative differences exist between the two approaches. The Pearson correlation coefficient between RRTM runs with ECMWF, and NRLMSIS-00 for $LW{\uparrow}_{CS}$, $LW{\downarrow}_{CS}$, $SW{\uparrow}_{CS}$, and $SW{\downarrow}_{CS}$ is greater than 99.2%.

2.4. CRE

The SW, LW, and net radiation at the surface (Q) are a combination of the broadband radiation components:

$$\begin{aligned} Q_{SW} &= SW_{\downarrow} - SW_{\uparrow} \\ Q_{LW} &= LW_{\downarrow} - LW_{\uparrow} \\ Q_{net} &= Q_{SW} + Q_{LW} \end{aligned} \tag{1}$$

From this, SW, LW and net CRE are calculated as

$$\begin{aligned} CRE_{SW} &= Q_{SW_{All\ Sky}} - Q_{SW_{Clear\ Sky}} \\ CRE_{LW} &= Q_{LW_{All\ Sky}} - Q_{LW_{Clear\ Sky}} \\ CRE_{net} &= Q_{net_{All\ sky}} - Q_{net_{Clear\ Sky}} \end{aligned} \tag{2}$$

Note that broadband radiation measurements and CRE are full hemispheric measurements, while measurements from CAPABL, MWR, and P-AERI are column/point measurements. As described below, measurements of more consistent scenes (e.g., clear-sky or overcast) provide the most definitive interpretation.

2.5. Assessing Radiative Impacts of HOIC

Two examples of CAPABL data are given to illustrate both the data available and the function of the ancillary data to clarify and remove contradictory data. Here, we show 2 days that illustrate all the data filters, as no single day clearly shows all the filters implemented. A typical observation set is given in Figure 1 for 3 October 2016 and, in Appendix B, Figure B1 for 22 August 2016.

To assess the radiative impacts of HOIC on the surface, CAPABL observations are used to categorize the derived CRE data by atmospheric scene type: clear-air, mixed-phase, ROIC, and HOIC. The range resolved data classification (Figure 1A) identifies ice clouds for most of the day with precipitating mixed-phase clouds in the middle of the day. Two modes of HOIC are observed throughout the 2-year data set: one being a large organized layer, seen in Figure 1, spanning approximately 2 hr and 4 km (similar to the event shown in Neely et al., 2013), and many shorter sporadic events spanning no more than a few minutes and less than 100 m (similar to those shown in Stillwell et al., 2018, in their Figures 1 and 2). Using CAPABL, we are

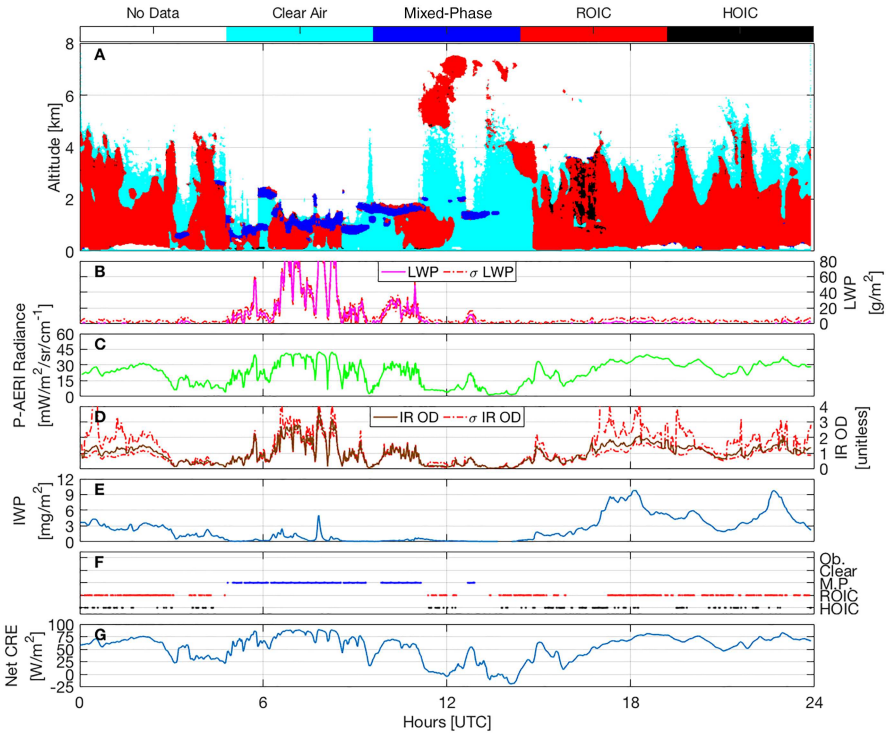

Figure 1. Representative data from 3 October 2016. (A) CAPABL's classified observations, (B) LWP and error estimate (σ LWP), (C) P-AERI 10.4 μm radiance, (D) infrared OD (IR OD) with bounds (σ IR OD) from cloud top and bottom temperatures, (E) IWP, (F) refined CSCI without 3-hour consistency filter, and (G) net CRE. Note that P-AERI radiance errors are <1% of the measured radiance in all cases and are not plotted for readability.

able to establish whether a voxel of ice crystals is dominated by HOIC. As such, these results are a conservative estimate of the occurrence and impact of HOIC on CRE, because voxels that contain HOIC but whose scattering is not dominated by HOIC are classified as ROIC. Though they are different in spatial and temporal extent, it is important to note that both sets pass the same extensive data quality procedures described in Stillwell et al. (2018).

The CSCI collapses the range resolved classification into the scene types versus time. The CSCI based on CAPABL data are refined using observations from the MWR (Figure 1B) and observations and derived

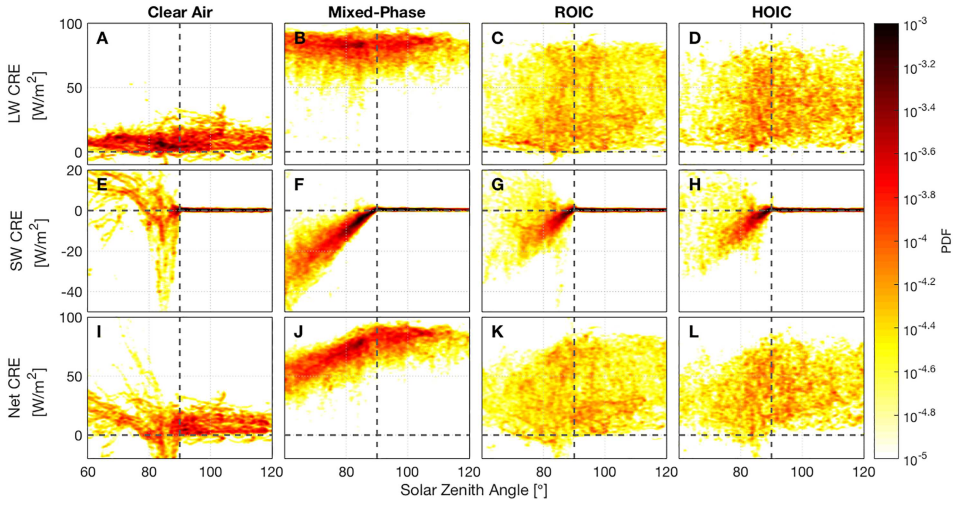

Figure 2. Bivariate PDFs of CRE components by classification type as a function of SZA. Positive net CRE equates to warming of the surface. Note the y-scale difference for each row.

products from the P-AERI (Figure 1C and Figure 1 D). Contradictory data are removed (Figure 1F). Inconsistent data can be observed between CAPABL and the MWR-derived LWP in multiple ways. First, during precipitation events, when CAPABL's signal is strongly attenuated by precipitation and cannot observe regions of the cloud dominated by liquid (typically at cloud top), CAPABL can observe only ice precipitation, while the MWR observed liquid water. This is observed between ~20 and 24 UTC in Figure B1. Second, CAPABL can observe liquid, while the MWR does not in two scenarios. The first such scenario is mixed-phase clouds occurring without large portions of liquid water, as is shown between ~3 and 4 UTC or ~12 and 14 UTC on Figure 1. The second scenario is voxels with high backscatter coefficient but low depolarization ratio. This can either indicate particular aerosol layers, not shown here, or indicate inhomogeneous voxels whose scattering is dominated by ice but whose depolarization signal is contaminated by clear-air. This is observed after approximately 14 UTC sporadically in Figure 1. Further contradictions can occur, for example, when optically thin diamond dust or fog, below CAPABL's observable range, are observed by P-AERI, which is observed between ~12 and 13 UTC in Figure B1. Additionally, as mentioned above, cloud layers with IR OD unambiguously above 1.5, that is, all IR OD calculated with cloud top, middle, and bottom are above 1.5, are removed to avoid the possibility of not observing an entire ice cloud. All contradictions are removed, but if no data exists, either through data agreement or lack of ancillary data due to instrument downtime, to refute the CSCI, it is used without modification.

The final filter is applied to better compare point/column and full hemispheric measurements. A 3-hr window is used to filter measurements (not applied in Figure 1 or Figure B1 for illustrative purposes). If a measurement of a certain type does not occur more than half of the time in a given window, it is discarded. For the period of interest (July 2015 to June 2017), the MWR, P-AERI, OD (ice clouds removed with OD > 1.5), and running average filter removed 9.2%, 4.6%, 3.2%, and 25.2% of data columns, respectively. Combined, they remove 35.6% of the data as some measurements are removed by more than one filter. Using the refined CSCI, the derived CRE (Figure 1G) values are assigned a category for all available data.

3. Results

The refined CSCI indicates clear-air, aerosols, mixed-phase, ROIC, HOIC, and obscured data occur 6.5%, 4.0%, 13.1%, 20.3%, 7.0%, and 13.5% percent of the time, respectively. The remaining 35.6% is removed as described above by data filtering. HOIC occur in at least 25.6% of all observed ice-only columns, the sum of ROIC, and HOIC occurrence. By volume, HOIC is composed of ~1.4% of all ice voxel observations (a lower limit based on the above described scattering and measurement sensitivity).

To summarize the 2 years of CRE categorization, bivariate probability distribution functions (2-D PDFs) are calculated for each categorization type as a function of CRE and SZA for the net SW and LW radiative components as well as the total CRE, shown in Figure 2. In general, LW CRE is expected to be a weak function of SZA through secondary surface and atmospheric temperature effects, and SW CRE is expected to be a strong function of SZA tending to zero for SZA > 90^o. This dependence is quantified by performing a linear regression on the maximum values of the 2-D PDF for each SZA, using values with occurrence frequency above $10^{-4.05}$ yielding a line-fit slope with units of W/m^2 per SZA^o. This is used as a proxy for cloud albedo, which the authors cannot measure directly. For LW and net CRE, all SZAs are used; for SW only SZA < 90^o is used.

Clear-air CRE for both SW and LW should be approximately 0 for all SZA. For LW CRE, the occurrence frequency reaches its maximum near zero CRE for all SZA (Figure 2A). The occurrence of nonzero SW CRE values for clear-air increases as SZA approaches 90^o indicating a difficulty in comparing point measurements to full hemispheric measurements especially with glancing solar rays (Figure 2E). Increasing the time interval over which to apply the consistency filter limits this effect at the expense of data availability for analysis. Clear-air net CRE shows a weak SZA dependence (slope of 0.14 ± 0.02 $W/m^2/SZA^o$) as Summit has high surface albedo year-round (Figure 2I). Summit does not experience major changes in surface albedo throughout the year (like melting sea ice), but Miller et al. (2015) show a minor dependence of surface albedo on SZA.

No SZA dependence on LW CRE is observed for mixed-phase clouds (Figure 2B; slope of -0.01 ± 0.01 $W/m^2/SZA^o$) with a median of approximately 85 W/m^2. Both mixed-phase and clear-air show single mode behavior in the LW that has been observed by previous studies (e.g., Shupe & Intrieri, 2004). A strong SZA dependence is observed in the SW confirming previous studies discussed in section 1 that indicate cooling

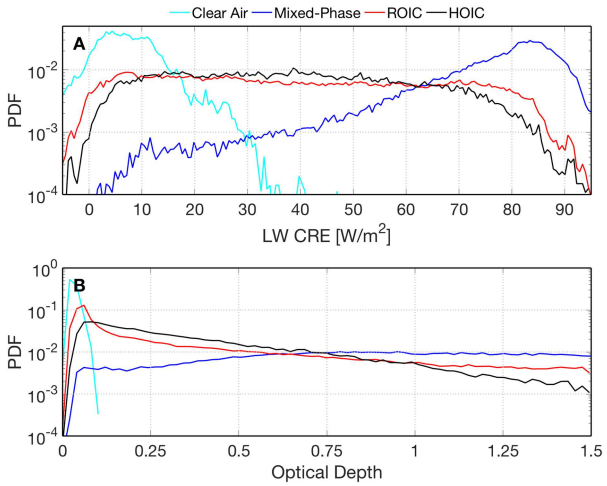

Figure 3. Univariate PDFs of the LW CRE (Panel A) and cloud IR OD (Panel B). All possible LW CRE and IR OD data are presented that have a valid refined CSCI identification.

effects of clouds are more prominent in summer with minimum SZA (Figure 2F). Net CRE for mixed-phase clouds is strongly positive for all SZAs observed at Summit (Figure 2 J), as observed by Miller et al. (2015).

Clouds containing ROIC and HOIC, in contrast to clear-air and mixed-phase clouds, display a much larger range and variation of CRE values for a given SZA. Both ROIC and HOIC show no clear LW CRE dependence on SZA (Figures 2C and 2D) and show similar SW effects to mixed-phase clouds (Figures 2G and 2H). As SZA decreases from 90°, the maximum observed net CRE decreases (Figures 2K and 2L).

A strong SZA dependence is seen in Figures 2F–2H. Slopes of 1.08 ± 0.01, 0.82 ± 0.04, and 1.02 ± 0.05 W/m^2/SZA^o are observed for mixed-phase, ROIC, and HOIC, respectively. This result indicates that for a given SZA, mixed-phase clouds reflect more SW energy than ice clouds, which is well known in the Arctic (e.g., Curry et al., 1996). It also indicates that for a given SZA, clouds containing HOIC reflect more SW energy than those containing strictly ROIC, by 21.7 % ± 9.7%, which has been hypothesized (e.g., Hirakata et al., 2014; Takano & Liou, 1989) but, to our knowledge, not been previously observed. These results also lend confidence that the HOIC observations are reasonable.

Further analysis on LW data not showing strong SZA dependence is performed by integrating across SZA. Figure 3A depicts PDFs of the net LW CRE summed across all SZAs, and Figure 3B depicts PDFs of the cloud IR OD. As described for Figure 2A and Figure 2B, clear-air and mixed-phase categories dominate the extremes of the LW CRE, while ice clouds are more evenly distributed. However, ROIC and HOIC show different LW behaviors with ROIC indicating a bimodal behavior with corresponding local maxima near clear-air and mixed-phase maxima. Using the LW CRE data from both ROIC and HOIC distributions and applying the two-sample Kolmogorov-Smirnov test (Marsaglia et al., 2003; Massey, 1951; Miller, 1956), to evaluate the null hypothesis that the two sets of data come from the same continuous probability distribution, results in the rejection of that hypothesis at the $p < 0.01$ confidence level. The difference between the PDFs of ROIC and HOIC peaks at nearly a factor of 2 at ~40 W/m^2. Similarly, the two-sample Kolmogorov-Smirnov test also rejects the same null hypothesis for IR OD at the $p < 0.01$ confidence level. Note here that IR OD should not be compared to the SW CRE described above. OD in the visible portion of the spectrum is not calculated.

Importantly, the results for LW CRE and IR OD show the same behavior originating from two nearly independent data sources. CRE is a hemispheric parameter calculated with broadband radiation measurements and calculated RRTM clear-sky radiances, and IR OD is a column measurement using a clear microwindow at 10.4 μm. The only link between these products is radiosonde-derived temperatures. While all the data presented have distinct error sources, the consistent behavior from nearly independent data sets lends confidence to the conclusion presented, as no systematic error source or error covariance is present. Clear-air columns have a single peak near zero CRE (IR OD) that falls quickly as LW CRE (IR OD) increases. CRE decreases more slowly as it is a hemispheric parameter, whereas IR OD is a column measurement more accurately classified by the CSCI. The PDF of mixed-phase columns increases with increasing CRE (IR OD) to a maximum near a state indicative of black-body radiation. The PDFs of ROIC and HOIC intersect twice with HOIC greater for the middle of the range of observations. For thin clouds, defined here as clouds with IR OD ≤ 1, the median of LW CRE for layers containing HOIC (34.8 W/m^2) is 8% higher than that of ROIC (32.0 W/m^2).

4. Discussion

One possible explanation for the difference in LW CRE (Figure 3A) and IR OD (Figure 3B) is differences in the IWP of the cloud columns over the time period of interest, that is, HOIC and ROIC could occur in columns with different average IWP. To evaluate this possibility for the entire data set, IWP PDFs are shown in Figure 4 for all columns with IR OD < 1.5. We again perform a two-sample Kolmogorov-Smirnov test applied to the IWP PDF. This test fails to reject the null hypothesis that the two sets of data come from

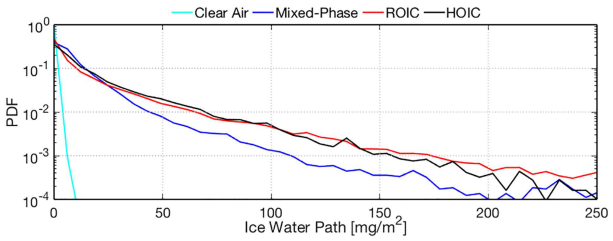

Figure 4. Univariate PDF of the IWP for all clouds observed with IR OD < 1.5. All possible IWP data is presented that has a valid refined CSCI identification.

the same continuous probability distribution (p value of 0.68). This test shows that while CRE and IWP are strongly related, the differences in CRE cannot be attributed to differences in IWP in this case in a statistically significant manner.

A second possible explanation for the differences in CRE and IR OD is differences in the vertical distribution of ice and by extension the emission temperature of the cloud layers. To evaluate this dependency, we calculate both layer median temperatures and the average vertical distribution of IWC.

We use the temperatures described in section 2.1 from radiosonde profiles and MWR data. Each layer's temperature is calculated and categorized by the refined CSCI. We take a median of all layers over the 2-year study for a given IR OD for a given column type. Because of the difficulty in ascribing a temperature to a layer that is not optically thick, we analyze temperature at cloud base (not shown), cloud median altitude shown in Figure 5, and cloud top (not shown). Note that these temperatures are ascribed to each column and not each voxel to evaluate the entire layer emission. HOIC layers are either equal in temperature or colder than ROIC layers for the majority of the IR OD range. This finding, found at cloud median altitude, does not change using the results at cloud top or cloud bottom. Similar to the result for IWP, while CRE and cloud temperature are strongly related, cloud emission temperature cannot explain the differences in CRE and IR OD between layers containing HOIC and those with only ROIC. In fact, the colder temperature of HOIC layers indicates the need to identify an enhancement mechanism associated with HOIC that is elevating LW CRE. Note that similar conclusions have be drawn using IWP as an independent variable instead of OD (not shown).

Another possibility to explain the observed difference in ROIC and HOIC LW effects is a difference in the vertical distribution of ice. It is possible that the actual vertical distribution of ice is not similar between the two classes and complicates the above argument about cloud temperature. To address this possibility, we take the IWC calculated with the MMCR data and determine an average profile of IWC per classification for the entire 2-year period. The result is shown in Figure 6. From Figure 6, we determine that no fundamental difference in the vertical distribution of ROIC and HOIC capable of explaining an enhanced LW CRE is visible. In fact, as with temperature, we find a contradictory physical effect where HOIC exist at higher altitudes on average (i.e., longwave emission at higher/colder temperatures should be reduced). The altitude of the median IWC value of ROIC and HOIC is at 1.2 km and 1.5 km, respectively. This reinforces the temperature analysis and leads us to conclude that the vertical distribution of IWC likely does not explain the differences we observe in the LW CRE of ROIC and HOIC. Yet, the issues with accurately making observations that represent the full distribution of IWC throughout the atmosphere and determining whether these distributions contain HOIC does not preclude this possibility.

As the results of this study are dependent on observations, it is important to address any possible biases that the measurements may have introduced and are influence our interpretation of the observed cloud properties. Two important errors to address are those associated with the retrievals of IWC and IR OD. IWC retrievals have large errors, originating from the assumed power-law relationship between IWC and radar reflectivity, in general. However, it should be noted that these errors are not expected to correlate with ice crystal orientation as the radar wavelength is not small compared to the scatterers (Rayleigh scattering). These errors cause no systematic bias over the 2-year period of interest and do not affect the conclusions described relating to the effect of IWC/IWP on LW CRE. IR OD errors originate primarily from uncertainty in the exact emission temperature of observed clouds. We bound these errors with the extreme temperatures of the cloud edges. Using these extreme values of IR OD, we also find no change in the relationship between enhanced LW CRE and clouds containing HOIC relative to clouds lacking HOIC.

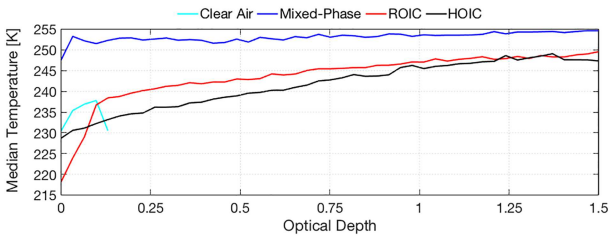

Figure 5. Cloud layer median temperatures at geometric median altitude for all layers with a given optical depth. There are 50 IR OD bins for a width of 0.03 per measurement. Note that clear-air is not observed with IR OD beyond 0.1. All possible IR OD data are presented that have a valid refined CSCI identification.

LW CRE is a combination of emitted energy originating from the cloud layer and surface energy scattered by the cloud layer. The observed IR

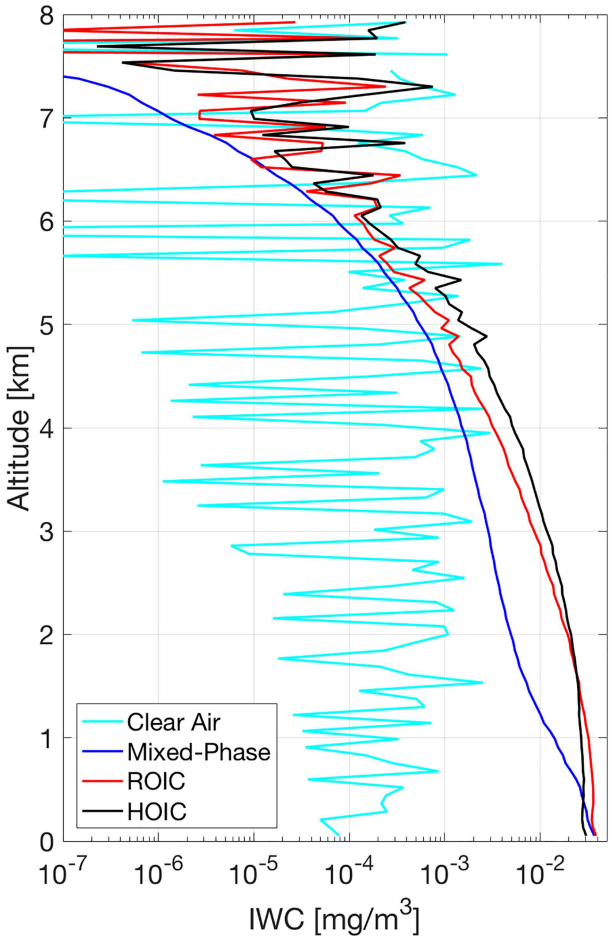

Figure 6. Average vertical distribution of IWC divided by classified lidar data. All possible IWC data are presented that have a valid refined CSCI identification.

OD is also a combination of emitted energy and scattered surface energy. Cloud emission and atmospheric emission can be parsed by way of a clear microwindow in the P-AERI spectrum. It is important to note, however, that surface emission scattered by clouds is not parsed from cloud emission in this way and was assumed to be zero. In this way, LW CRE and IR OD are different only in the field of view. We show that the LW CRE and the observed IR OD for ROIC and HOIC are statistically different, but that IWP is not. We also note that while the voxel temperature of HOIC and ROIC are statistically different (not shown), the median layer temperature, an estimate of the emission temperature, is higher for ROIC than for HOIC. Thus, both primary drivers of cloud LW emission (temperature and IWC) fail to conclusively explain the differences observed in Figure 3.

Two possibilities for the enhanced CRE of clouds containing HOIC compared to clouds containing strictly ROIC. First, the difference could be related to differences in populations of ROIC crystals, that is, clouds that have higher CRE also contain HOIC more frequently or have conditions that favor the formation of HOIC. Second, HOIC could be causing the observed differences directly. The data presented, specifically the failure of two-sample Kolmogorov-Smirnov test applied to the IWP distributions and the colder emission temperatures of clouds containing HOIC compared to those containing strictly ROIC, lead us to favor the latter conclusion.

Due to the incoherent nature of thermal emission, there is no physical mechanism known to the authors that would alter the emission spectrum of the clouds based on crystal orientation. Therefore, the difference could be due to scattering of surface LW emission, observed in both LW CRE and IR OD measurements. Ice crystal diameters in the Arctic range from ~100 μm to several millimeters indicating that the interaction of radiation with the crystals in both SW and LW are well outside the Rayleigh regime (where one would expect no functional dependence of scattered light on orientation). Enhanced LW CRE by HOIC is not observed in the limit of CRE as it approaches zero indicating that this mechanism is less prominent in clouds with very small OD (i.e., clouds with little scattering) or with small particles. As cloud IR OD increases, this effect is also minimized as black-body absorption/emission dominates. The same basic mechanism has been previously proposed (e.g., Takano & Liou, 1989) to enhance SW cloud albedo.

5. Conclusions

The importance of cloud microphysical properties on CRE is well established. Given the vulnerability of the GrIS to changes in CRE (e.g., Bennartz et al., 2013; Van Tricht et al., 2016), a better understanding of the linkages of cloud microphysical properties to CRE is needed. The lack of understanding of CRE is made prominent by its poor representation in climate models (e.g., Cawkwell & Bamber, 2002). Current simulations of climate and cloud radiative transfer rely on parameterizations of CRE, which commonly assume that the crystals within ice clouds are randomly oriented (Yang et al., 2005). At Summit from July 2015 to June 2017, HOIC occur in at least 25.6% of all data columns containing only ice or, as a lower limit, 1.4% of observed ice by volume. These observations indicate the inaccuracy of the ROIC assumption. These HOIC may directly affect surface and TOA radiative balance and have indirect effects through ice fall speed.

We present observations that, for the first time, suggest that clouds containing oriented ice crystals have altered both SW and LW CRE over a continuously high albedo surface in the Arctic. We find that the LW CRE and IR OD from clouds containing ROIC and HOIC fail the null hypothesis that they come from the

same continuous probability distribution function at the $p < 0.01$ confidence level. The results show that on average clouds containing HOIC enhance surface warming by approximately 8% due to the possible effects of enhanced LW opacity compared to clouds containing ROIC with IR OD ≤ 1, despite the fact that the HOIC containing clouds were observed to have lower average emission temperatures. We also find that clouds with HOIC have a SW CRE that increases faster as a function of SZA than clouds with only ROIC, increasing surface cooling effects by approximately 22%.

It remains unclear whether the observed differences are caused by the presence of HOIC or whether the cloud properties that result in the observed SW and LW CRE are also conducive to the occurrence of HOIC. We hypothesize that the enhancement of LW CRE is due to LW scattering by clouds containing HOIC (relative to clouds containing ROIC), a similar mechanism to that of SW enhancements. More research is needed to confirm, or refute, this hypothesis. However, regardless of the mechanism, these results clarify that observed clouds containing HOIC have increased (decreased) LW (SW) CRE (increased heating and increased cooling, respectively), implying that assuming all ice crystals in clouds are randomly oriented may result in low (high) biases in modeled LW (SW) CRE.

It should be noted that the relative importance of HOIC and ROIC on the SW and LW CRE of clouds is highly uncertain. Comparatively, the relative importance of HOIC in lidar observations is highly disproportionate. Zenith and nadir pointing lidar observations, which are particularly sensitive to the occurrence of HOIC, find several orders of magnitude difference (Platt et al., 1978; Sassen, 1980; Westbrook et al., 2010) in the observed signal strength between clouds containing only ROIC versus clouds containing HOIC. Such differences are known to cause biases in the estimates of cloud phase with lidar-based observations (e.g., Hu, 2007). However, it is unclear how to extend this well-accepted observation to assess the importance of HOIC on CRE, which is of importance to the wider community. As such, the importance of clouds containing HOIC might not be weighed by their occurrence frequency alone. To our knowledge, there are no tools currently available in the community to adequately model the relative impact of HOIC on CRE, especially in the LW. As such, the observations shown here provide motivation for the community to explore these differences more closely.

The robustness of these observational results across larger scales, that is, pan-Arctic or globally, also remains to be tested, and more research is required to evaluate the validity of these results at other sites and their implications for the TOA. We suggest that microphysical modeling of HOIC in the LW would aid the interpretation of the results presented, similar to those presented by Takano and Liou (1989) for the visible portion of the spectrum. We also suggest that future climate model studies explore atmospheric radiative transfer parameterizations that account for ice crystal orientation, facilitating a method to explore the global implications of how ice crystal orientation affects both SW and LW radiation at the surface.

Appendix A

The data quality control and data analysis for the CAPABL system are described in detail in Stillwell et al. (2018). Here we summarize the classification scheme presented in Stillwell et al. (2018; Table 2) with the flow chart given in Figure A1. First, CAPABL data is temporally and spatially integrated to increase the signal-to-noise ratio of the raw data. In this work, raw data are collected at approximately 6-m and 5-s resolution and are integrated to 25-m and 82-s resolution. Background photon counts are calculated and removed. This raw data are then passed through a signal-to-noise ratio filter and speckle filter (described in detail by Stillwell et al., 2018). This forms the Filtered CAPABL data used as a starting step in Figure A1. Data that are available can be used to then calculate both backscatter ratio, using a Klett style inversion, and polarization properties. Error estimates of polarization properties are also calculated. With these quantities calculated, the base classification scheme is as shown in Figure A1. Note that all nonphysical values of backscatter ratio and polarization variables as well as variables with unacceptably high error bounds are removed as described by Stillwell et al. (2018).

Note that the detailed implementation of this scheme including merging of analog and photon counting data streams as well as orthogonal and nonorthogonal polarization calculations is detailed in Stillwell et al. (2018).

The base classified data from CAPABL are used to for the base CSCI as shown in Figure A2. This simple version of a column mask is then refined using ancillary measurements. The refinement of the base CSCI is preformed as in Figure A3. Contradictions are removed as well as any data that fail quality control measured implemented in previous steps.

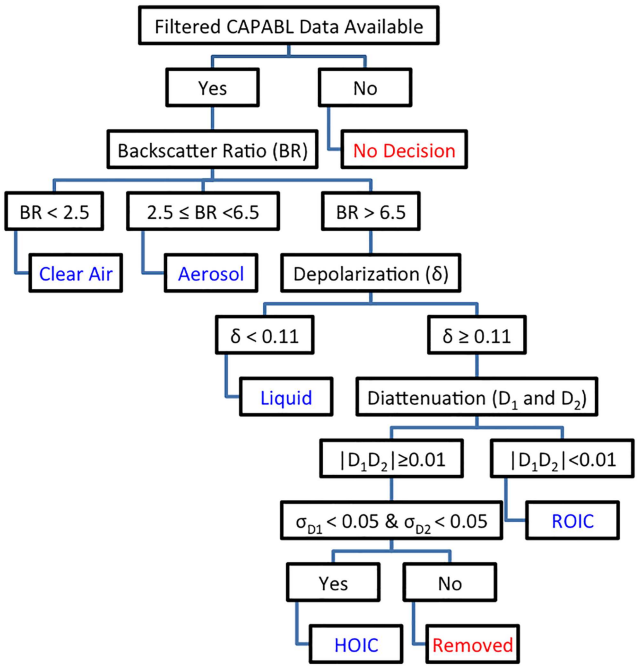

Figure A1. Flow chart describing the CAPABL base identification.

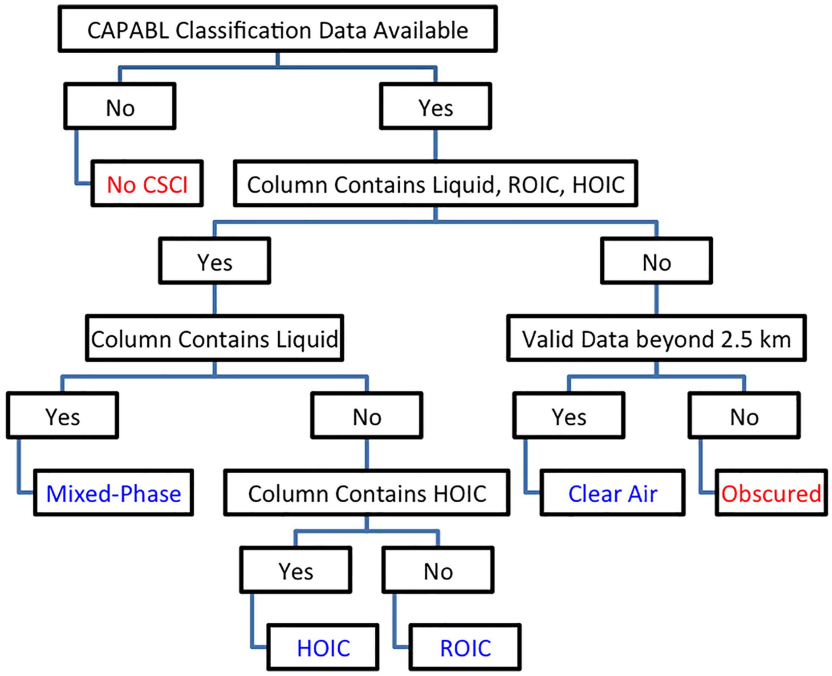

Figure A2. Flow chart describing the base CSCI.

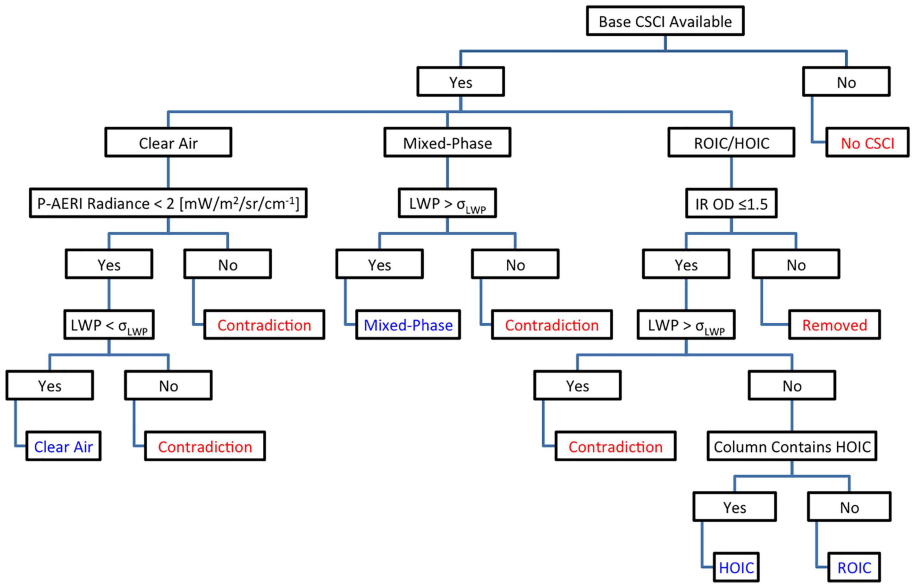

Figure A3. Flow chart describing the refinement of the CSCI with ancillary instrumentation.

Appendix B

A second data set used to further illustrate some of the filtering steps is described in section 2.5. In particular, the LWP filter removes false-positive mixed-phase identifications before noon on this day and false ROIC observations in a clear mixed-phase region after 20 UTC. Further, the P-AERI filter removes false-positive

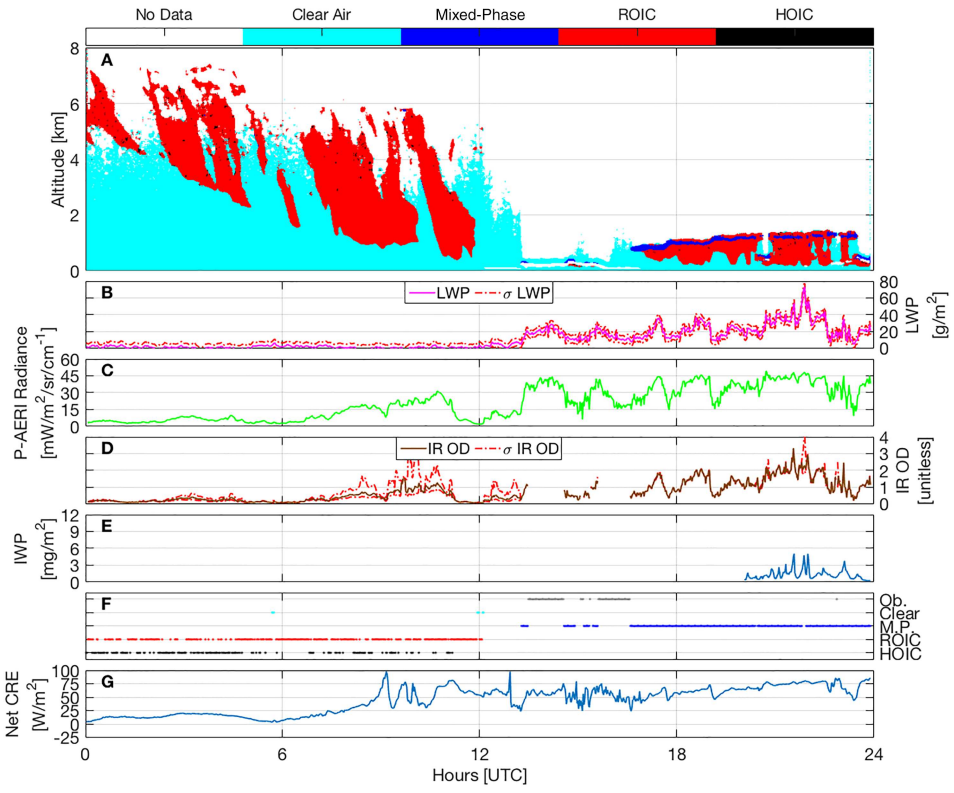

Figure B1. Same as Figure 1 for 22 August 2016. Note that IWP is not presented for the entire day because the MMCR was not operational from 0 to 20 UTC on this day.

clear-air identifications near noon. Finally, this data clearly shows obscured CAPABL data that is identified from approximately 13 to 16 UTC due to low-level fog.

Acknowledgments
This material is based upon work supported by the NSF Graduate Research Fellowship Program under Grant No. DGE 1144083 and NSF Grants PLR-1303864, PLR-1303879, PLR-1314156, and ATM-0454999. The National Center for Atmospheric Research is funded by the National Science Foundation (NSF). Ryan Neely is funded by the National Centre for Atmospheric Science. Observations collected as part of ICECAPS are available at the NSF Arctic Data Center website (https://arcticdata.io/catalog/#view/urn:uuid:f783f072-e5e0-454c-9c9d-136935e1cb7c). Penny Rowe and Christopher Cox helped perform calibration of the data from the Polar Atmospheric Emitted Radiance Interferometer. David Turner and Claire Pettersen performed the microwave radiometer retrievals. Data provided by GMD is available online (www.esrl.noaa.gov/gmd/dv/ftpdata.html). All authors would like to especially thank the staff and science technicians at Summit Station as well as the entire team at Polar Field Services for their support and dedication to help maintain the instrumentation and collect the data presented in this work. The authors also thank Scott Spuler and Matthew Hayman for their thoughtful and constructive comments in compiling this manuscript.

References

Bennartz, R., Shupe, M. D., Turner, D. D., Walden, V. P., Steffen, K., Cox, C. J., et al. (2013). July 2012 Greenland melt extent enhanced by low-level liquid clouds. *Nature*, *496*(7443), 83–86. https://doi.org/10.1038/nature12002

Bréon, F.-M., & Dubrulle, B. (2004). Horizontally oriented plates in clouds. *Journal of the Atmospheric Sciences*, *61*(23), 2888–2898. https://doi.org/10.1175/JAS-3309.1

Cadeddu, M. P., Liljegren, J. C., & Turner, D. D. (2013). The Atmospheric radiation measurement (ARM) program network of microwave radiometers: instrumentation, data, and retrievals. *Atmospheric Measurement Techniques*, *6*(9), 2359–2372. https://doi.org/10.5194/amt-6-2359-2013

Cawkwell, F., & Bamber, J. L. (2002). The impact of cloud cover on the net radiation budget of the Greenland ice sheet. *Annals of Glaciology*, *34*(1), 141–149. https://doi.org/10.3189/172756402781817789

Chen, T., Rossow, W. B., & Zhang, Y. (2000). Radiative effects of cloud-type variations. *Journal of Climate*, *13*(1), 264–286. https://doi.org/10.1175/1520-0442(2000)013<0264:REOCTV>2.0.CO;2

Clough, S. A., Shephard, M. W., Mlawer, E. J., Delamere, J. S., Iacono, M. J., Cady-Pereira, K., et al. (2005). Atmospheric radiative transfer modeling: a summary of the AER codes. *Journal of Quantitative Spectroscopy and Radiative Transfer*, *91*(2), 233–244. https://doi.org/10.1016/j.jqsrt.2004.05.058

Corti, T., & Peter, T. (2009). A simple model for cloud radiative forcing. *Atmospheric Chemistry and Physics*, *9*(15), 5751–5758. https://doi.org/10.5194/acp-9-5751-2009

Cox, C. J., Turner, D. D., Rowe, P. M., Shupe, M. D., & Walden, V. P. (2014). Cloud microphysical properties retrieved from downwelling infrared radiance measurements made at Eureka, Nunavut, Canada (2006–09). *Journal of Applied Meteorology and Climatology*, *53*(3), 772–791. https://doi.org/10.1175/JAMC-D-13-0113.1

Curry, J. A., & Ebert, E. E. (1992). Annual cycle of radiation fluxes over the Arctic Ocean: Sensitivity to cloud optical properties. *Journal of Climate*, *5*(11), 1267–1280. https://doi.org/10.1175/1520-0442(1992)005<1267:ACORFO>2.0.CO;2

Curry, J. A., Schramm, J. L., Rossow, W. B., & Randall, D. (1996). Overview of Arctic cloud and radiation characteristics. *Journal of Climate*, *9*, 1731–1764. https://doi.org/10.1175/1520-0442(1996)009<1731:OOACAR>2.0.CO;2

Dlugokencky, E. J., Lang, P. M., Mund, J. W., Crotwell, A. M., Crotwell, M. J., & Thoning, K. W. (2017). Atmospheric carbon dioxide dry air mole fractions from the NOAA ESRL Carbon Cycle Cooperative Global Air Sampling Network, 1968-2016, Version: 2017-07-28. ftp://aftp.cmdl.noaa.gov/data/trace_gases/co2/flask/surface/

Field, P. R., Hogan, R. J., Brown, P. R. A., Illingworth, A. J., Choularton, T. W., Kaye, P. H., et al. (2004). Simultaneous radar and aircraft observations of mixed-phase cloud at the 100 m scale. *Quarterly Journal of the Royal Meteorological Society*, *130*(600), 1877–1904. https://doi.org/10.1256/qj.03.102

Foster, T. C., & Hallett, J. (2002). The alignment of ice crystals in changing electric fields. *Atmospheric Research*, *62*(1-2), 149–169. https://doi.org/10.1016/S0169-8095(02)00008-X

Hashino, T., Chiruta, M., Polzin, D., Kubicek, A., & Wang, P. K. (2014). Numerical simulation of the flow fields around falling ice crystals with inclined orientation and the hydrodynamic torque. *Atmospheric Research*, *150*, 79–96. https://doi.org/10.1016/j.atmosres.2014.07.003

Hayman, M., Spuler, S., & Morley, B. (2014). Polarization lidar observations of backscatter phase matrices from oriented ice crystals and rain. *Optics Express*, *22*(14), 16,976–16,990. https://doi.org/10.1364/OE.22.016976

Hayman, M., Spuler, S., Morley, B., & VanAndel, J. (2012). Polarization lidar operation for measuring backscatter phase matrices of oriented scatterers. *Optics Express*, *20*(28), 29,553–29,567. https://doi.org/10.1364/OE.20.029553

Hayman, M., & Thayer, J. P. (2012). General description of polarization in lidar using Stokes vectors and polar decomposition of Mueller matrices. *J. Opt. Soc. Am. A, JOSAA*, *29*(4), 400–409. https://doi.org/10.1364/JOSAA.29.000400

Hedin, A. E. (1985). Extension of the MSIS thermospheric model into the middle and lower atmosphere. *Journal of Geophysical Research*, *96*, 1159.

Hess, M., & Wiegner, M. (1994). COP: a data library of optical properties of hexagonal ice crystals. *Applied Optics*, *33*(33), 7740–7746. https://doi.org/10.1364/AO.33.007740

Hirakata, M., Okamoto, H., Hagihara, Y., Hayasaka, T., & Oki, R. (2014). Comparison of global and seasonal characteristics of cloud phase and horizontal ice plates derived from CALIPSO with MODIS and ECMWF. *Journal of Atmospheric and Oceanic Technology*, *31*(10), 2114–2130. https://doi.org/10.1175/JTECH-D-13-00245.1

Hogan, R. J., Francis, P. N., Flentje, H., Illingworth, A. J., Quante, M., & Pelon, J. (2003). Characteristics of mixed-phase clouds. I: Lidar, radar and aircraft observations from CLARE'98. *Quarterly Journal of the Royal Meteorological Society*, *129*(592), 2089–2116. https://doi.org/10.1256/rj.01.208

Hu, Y. (2007). Depolarization ratio-effective lidar ratio relation: Theoretical basis for space lidar cloud phase discrimination. *Geophysical Research Letters*, *34*, L11812. https://doi.org/10.1029/2007gl029584

Intrieri, J., Shupe, M. D., Uttal, T., & McCarty, B. J. (2002). An annual cycle of Arctic cloud characteristics observed by radar and lidar at SHEBA. *Journal of Geophysical Research*, *107*(C10), 8030. https://doi.org/10.1029/2000jc000423

Ji, W., & Wang, P. K. (1999). Ventilation coefficients for falling ice crystals in the atmosphere at low-intermediate Reynolds numbers. *Journal of the Atmospheric Sciences*, *56*(6), 829–836. https://doi.org/10.1175/1520-0469(1999)056<0829:VCFFIC>2.0.CO;2

Kajikawa, M. (1992). Observations of the falling motion of plate-like snow crystals Part I: The free-fall patterns and velocity, Journal of the Meteorological Society of Japan. *Ser. II*, *70*(1), 1–9. https://doi.org/10.2151/jmsj1965.70.1_1

Kay, J. E., & L'Ecuyer, T. (2013). Observational constraints on Arctic Ocean clouds and radiative fluxes during the early 21st century. *Journal of Geophysical Research: Atmospheres*, *118*, 7219–7236. https://doi.org/10.1002/jgrd.50489

Keat, W. J., & Westbrook, C. D. (2017). Revealing layers of pristine oriented crystals embedded within deep ice clouds using differential reflectivity and the copolar correlation coefficient. *Journal of Geophysical Research: Atmospheres*, *122*, 11–737–11–759. https://doi.org/10.1002/2017JD026754

Klett, J. D. (1995). Orientation model for particles in turbulence. *Journal of the Atmospheric Sciences*, *52*(12), 2276–2284. https://doi.org/10.1175/1520-0469(1995)052<2276:OMFPIT>2.0.CO;2

Knuteson, R. O., Revercomb, H. E., Best, F. A., Ciganovich, N. C., Dedecker, R. G., Dirkx, T. P., et al. (2004a). Atmospheric emitted radiance interferometer. *Part I: Instrument design, Journal of Atmospheric and Oceanic Technology*, *21*(12), 1763–1776. https://doi.org/10.1175/jtech-1662.1

Knuteson, R. O., Revercomb, H. E., Best, F. A., Ciganovich, N. C., Dedecker, R. G., Dirkx, T. P., et al. (2004b). Atmospheric emitted radiance interferometer. Part II: Instrument performance. *Journal of Atmospheric and Oceanic Technology*, *21*, 1777–1789. https://doi.org/10.1175/JTECH-1663.1

Labitzke, K., Barnett, J. J., & Edwards, B. (Eds.) (1985). Middle Atmosphere Program. Handbook for MAP. Volume 16: Atmospheric Structure and Its Variation in the Region 20 to 120 Km. Draft of a New Reference Middle Atmosphere.

Marsaglia, G., Tsang, W., & Wang, J. (2003). Evaluating Kolmogorov's Distribution. *Journal of Statistical Software*, *8*(18). https://doi.org/10.18637/jss.v008.i18

Massey, F. J. (1951). The Kolmogorov-Smirnov Test for Goodness of Fit. *Journal of the American Statistical Association*, *46*, 68–78.

Matus, A. V., & L'Ecuyer, T. S. (2017). The role of cloud phase in Earth's radiation budget. *Journal of Geophysical Research: Atmospheres*, *122*, 2559–2578. https://doi.org/10.1002/2016JD025951

McClatchey, R. A., Fenn, R. W., Selby, J. E. A., Volz, F. E., & Garing, J. S. (1972). *Optical properties of the atmosphere. Rep. AFCRL-72-0497*. Bedford, MA: Hanscom Air Force Base.

Miller, L. H. (1956). Table of Percentage Points of Kolmogorov Statistics. *Journal of the American Statistical Association*, *51*(273), 111–121.

Miller, N. B., Shupe, M. D., Cox, C. J., Walden, V. P, Turner, D. D., & Steffen, K. (2015). Cloud Radiative Forcing at Summit, Greenland. *28*(15), 6267–6280. https://doi.org/10.1175/JCLI-D-15-0076.1

Miller, N. B., Turner, D. D., Bennartz, R., Shupe, M. D., Kulie, M. S., Cadeddu, M., & Walden, V. P. (2013). Surface-based inversions above central Greenland. *Journal of Geophysical Research: Atmospheres*, *118*, 495–506. https://doi.org/10.1029/2012JD018867

Mlawer, E. J., Taubman, S. J., Brown, P. D., Iacono, M. J., & Clough, S. A. (1997). RRTM, a validated correlated-k model for the longwave. *Journal of Geophysical Research*, *102*, 16,663–16,682.

Morrison, H., de Boer, G., Feingold, G., Harrington, J., Shupe, M. D., & Sulia, K. (2012). Resilience of persistent Arctic mixed-phase clouds. *Nature Geoscience*, *5*(1), 11–17. https://doi.org/10.1038/ngeo1332

Neely, R. R. III, Hayman, M., Stillwell, R., Thayer, J. P., Hardesty, R. M., O'Neill, M., et al. (2013). Polarization lidar at Summit, Greenland, for the detection of cloud phase and particle orientation. *Journal of Atmospheric and Oceanic Technology*, *30*(8), 1635–1655. https://doi.org/10.1175/JTECH-D-12-00101.1

NOAAGRAD (2017). Radiation Archive, Summit Observatory, Date Accessed: 2017-07-26, ftp://aftp.cmdl.noaa.gov/data/radiation/baseline/sum/

NOAAOZWV (2017). Vertical Ozone Profiles, Summit Observatory, Date Accessed: 2017-07-26, ftp://ftp.cmdl.noaa.gov//data/ozwv/Ozonesonde/Summit, Greenland/100 Meter Average Files/

Noel, V., & Chepfer, H. (2010). A global view of horizontally oriented crystals in ice clouds from Cloud-Aerosol Lidar and Infrared Pathfinder Satellite Observation (CALIPSO). *Journal of Geophysical Research*, *115*(D4), D00H23. https://doi.org/10.1029/2009JD012365

Picone, J. M., Hedin, A. E., Drob, D. P., & Aikin, A. C. (2002). NRLMSISE-00 empirical model of the atmosphere: Statistical comparisons and scientific issues. *Journal of Geophysical Research*, *107*(A12), 1468. https://doi.org/10.1029/2002JA009430

Platt, C. M. R., Abshire, N. L., & McNice, G. T. (1978). Some microphysical properties of an ice cloud from lidar observation of horizontally oriented crystals. *Journal of Applied Meteorology*, *17*, 1220–1224. https://doi.org/10.1175/1520-0450(1978)017<1220:SMPOAI>2.0.CO;2

Ramanathan, V., Cess, R. D., Harrison, E. F., Minnis, P., Barkstrom, B. R., Ahmad, E., & Hartmann, D. (1989). Cloud-radiative forcing and climate: Results from the Earth radiation budget experiment. *Science*, *243*(4887), 57–63. https://doi.org/10.1126/science.243.4887.57

Sassen, K. (1980). Remote sensing of planar ice crystal fall attitudes, Journal of the Meteorological Society of Japan. *Ser. II*, *58*(5), 422–429. https://doi.org/10.2151/jmsj1965.58.5_422

Sassen, K. (1984). Deep orographic cloud structure and composition derived from comprehensive remote sensing measurements. *Journal of Applied Meteorology*, *23*, 568–583. https://doi.org/10.1175/1520-0450(1984)023<0568:DOCSAC>2.0.CO;2

Sassen, K., Liou, K.-N., Takano, Y., & Khvorostyanov, V. I. (2003). Diurnal effects in the composition of cirrus clouds. *Geophysical Research Letters*, *30*(10), 1539. https://doi.org/10.1029/2003GL017034

Sassen, K., & Takano, Y. (2000). Parry arc: a polarization lidar, ray-tracing, and aircraft case study. *Applied Optics*, *39*(36), 6738–6745. https://doi.org/10.1364/AO.39.006738

Shupe, M. D. (2011). Clouds at Arctic atmospheric observatories, Part II: Thermodynamic phase characteristics. *Journal of Applied Meteorology and Climatology*, *50*(3), 645–661. https://doi.org/10.1175/2010jamc2468.1

Shupe, M. D., & Intrieri, J. (2004). Cloud radiative forcing of the Arctic surface: The influence of cloud properties, surface albedo, and solar zenith angle. *Journal of Climate*, *17*, 616–628. https://doi.org/10.1175/1520-0442(2004)017<0616:crfota>2.0.co;2

Shupe, M. D., Kollias, P., Persson, P. O. G., & McFarquhar, G. M. (2008). Vertical motions in Arctic mixed-phase stratiform clouds. *Journal of the Atmospheric Sciences*, *65*(4), 1304–1322. https://doi.org/10.1175/2007JAS2479.1

Shupe, M. D., Turner, D. D., Walden, V. P., Bennartz, R., Cadeddu, M. P., Castellani, B. B., et al. (2013). High and dry: New observations of tropospheric and cloud properties above the Greenland ice sheet. *Bulletin of the American Meteorological Society*, *94*(2), 169–186. https://doi.org/10.1175/BAMS-D-11-00249.1

Shupe, M. D., Uttal, T., & Matrosov, S. Y. (2005). Arctic cloud microphysics retrievals from surface-based remote sensors at SHEBA. *Journal of Applied Meteorology*, *44*, 1544–1562. https://doi.org/10.1175/JAM2297.1

Shupe, M. D., Walden, V. P., Eloranta, E., Uttal, T., Campbell, J. R., Starkweather, S. M., & Shiobara, M. (2011). Clouds at Arctic atmospheric observatories. Part I: Occurrence and macrophysical properties. *Journal of Applied Meteorology and Climatology*, *50*(3), 626–644. https://doi.org/10.1175/2010JAMC2467.1

Stillwell, R. A., Neely, R. R. III, Thayer, J. P., Shupe, M. D., & Turner, D. D. (2018). Improved cloud-phase determination of low-level liquid and mixed-phase clouds by enhanced polarimetric lidar. *Atmospheric Measurement Techniques*, *11*, 835–859. https://doi.org/10.5194/amt-11-835-2018

Sun, Z., & Shine, K. P. (1994). Studies of the radiative properties of ice and mixed-phase clouds. *Quarterly Journal of the Royal Meteorological Society*, *120*(515), 111–137. https://doi.org/10.1002/qj.49712051508

Takano, Y., & Liou, K. N. (1989). Solar radiative transfer in cirrus clouds. Part I: Single-scattering and optical properties of hexagonal ice crystals. *Journal of the Atmospheric Sciences*, *46*(1), 3–19. https://doi.org/10.1175/1520-0469(1989)046<0003:SRTICC>2.0.CO;2

Takano, Y., & Liou, K. N. (1993). Transfer of polarized infrared radiation in optically anisotropic media: application to horizontally oriented ice crystals. *J. Opt. Soc. Am. A, JOSAA*, *10*(6), 1243. https://doi.org/10.1364/josaa.10.001243

Thomas, L., & Cartwright, J. (1990). Lidar observations of the horizontal orientation of ice crystals in cirrus clouds. *Tellus B*, *42*(2), 211–216. https://doi.org/10.1034/j.1600-0889.1990.00001.x-i1

Tricker, R. A. R. (1971). *Introduction to meteorological optics, Introduction to meteorological optics*., by Tricker, R. A. R. London (UK): Mills and Boon, 286 p.

Turner, D. D., Clough, S. A., Liljegren, J. C., Clothiaux, E. E., Cady-Pereira, K., & Gaustad, K. L. (2007). Retrieving liquid water path and precipitable water vapor from atmospheric radiation measurement (ARM) microwave radiometers. *IEEE Transactions on Geoscience and Remote Sensing*, *45*, 3680–3690. https://doi.org/10.1109/TGRS.2007.903703

Van Tricht, K., Lhermitte, S., & Lenaerts, J. (2016). Clouds enhance Greenland ice sheet meltwater runoff. *Nat Comms*, *7*, 10266. https://doi.org/10.1038/ncomms10266

Vonnegut, B. (1965). Orientation of ice crystals in the electric field of a thunderstorm. *Weather*, *20*, 310–312.

Westbrook, C. D., Illingworth, A. J., O'Connor, E. J., & Hogan, R. J. (2010). Doppler lidar measurements of oriented planar ice crystals falling from supercooled and glaciated layer clouds. *Quarterly Journal of the Royal Meteorological Society*, *136*(646), 260–276. https://doi.org/10.1002/qj.528

Whipple, F. J. W. (1940). How are mock suns produced? *Quarterly Journal of the Royal Meteorological Society*, *66*(286), 275–280. https://doi.org/10.1002/qj.49706628603

Yang, P., Wei, H., Huang, H.-L., Baum, B. A., Hu, Y. X., Kattawar, G. W., et al. (2005). Scattering and absorption property database for nonspherical ice particles in the near- through far-infrared spectral region. *Applied Optics*, *44*(26), 5512–5523. https://doi.org/10.1364/AO.44.005512

Yoshida, R., Okamoto, H., Hagihara, Y., & Ishimoto, H. (2010). Global analysis of cloud phase and ice crystal orientation from Cloud-Aerosol Lidar and Infrared Pathfinder Satellite Observation (CALIPSO) data using attenuated backscattering and depolarization ratio. *Journal of Geophysical Research*, *115*, D00H32. https://doi.org/10.1029/2009JD012334

Zhou, C., Yang, P., Dessler, A. E., & Liang, F. (2013). Statistical properties of horizontally oriented plates in optically thick clouds from satellite observations. *IEEE Geoscience and Remote Sensing Letters*, *10*(5), 986–990. https://doi.org/10.1109/LGRS.2012.2227451